유연인쇄전자학술지, 2023년 6월, 제2권 제1호, pp. 119-143
Journal of Flexible & Printed Electronics, June 2023, Vol. 2, Issue 1, pp. 119-143
Received 2023-06-03, Revised 2023-06-18, Accepted 2023-06-29
https://doi.org/10.56767/jfpe.2023.2.1.119
eISSN: 2951-2174

RESEARCH

# Rhodanine-Based Non-Fullerene Acceptors for Organic Solar Cells with a High Open-Circuit Voltage of 1.07 V

Kwangmin Kim[1], BongSoo Kim[1,2,3*]

[1]Department of Chemistry, Ulsan National Institute of Science and Technology (UNIST), Ulsan, Korea
[2]Graduate School of Semiconductor Materials and Device Engineering,
Ulsan National Institute of Science and Technology (UNIST), Ulsan, Korea
[3]Graduate School of Carbon Neutrality, Ulsan National Institute of Science and Technology (UNIST), Ulsan, Korea

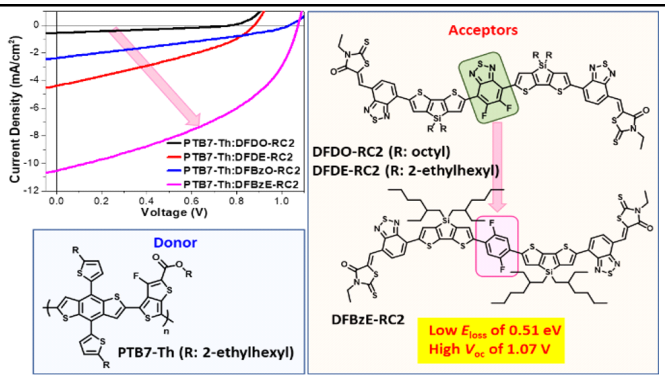


## ABSTRACT

To overcome the intrinsic limitations of fullerene-based organic photovoltaic (OPV) devices, research on OPV devices based on non-fullerene acceptors (NFAs) has been actively conducted in recent years. It is important to understand the relationship between the structure of the NFAs and photovoltaic properties to create high-performance OPV devices. In this study, we have designed and synthesized a series of NFAs (DFDO-RC2 and DFDE-RC2) based on electron-rich dithienosilole (D) and electron-deficient difluorobenzodiathiazole (F), benzodiathiazole-connected 3-ethylrhodanine (RC2) units, and alkyl chains of 2-ethylhexyl (E) and octyl (O) groups. The PTB7-Th:DFD-RC2 devices showed low PCEs mainly due to the highly located highest occupied molecular orbital (HOMO) energy levels of the DFD-RC2 acceptors compared to the PTB7-Th polymer donor. To lower the HOMO levels of the DFD-RC2 NFAs, the backbone structures were modified by replacing difluorobenzodiathiazole core moiety with difluorobenzene (FBz) to obtain DFBz-RC2 molecules (DFBzO-RC2 and DFBzE-RC2). PTB7-Th:DFBz-RC2 devices exhibited significantly improved PCEs compared to PTB7-Th:DFD-RC2 devices. The DFBzO-RC2 and DFBzE-RC2 molecule-based OPVs exhibited remarkably high $V_{oc}$s of 1.03 and 1.07 V, respectively, which characteristic is associated with the very low energy loss ($E_{loss}$) of 0.51 eV in both PTB7-Th:DFBzO-RC2 and PTB7-Th:DFBzE-RC2 devices. Overall, our investigation of the various synthesized molecules reveals the structure-to-photovoltaic properties, which guide the design of new high-performance NFAs to advance in the field of organic solar cells.

Key Words: Organic solar cells, Non-fullerene acceptors, Power conversion efficiency, Alkyl chain engineering

*Correspondence: bongsoo@unist.ac.kr

## 1. INTRODUCTION

Bulk heterojunction (BHJ) organic solar cells have heavily relied on fullerenes such as phenyl-$C_{61}$-butyric acid methyl ester ($PC_{61}BM$) and phenyl-$C_{71}$-butyric acid methyl ester ($PC_{71}BM$) for the past two decades, with their unrivaled electron-acceptor properties: good solubility in organic solvents, high electron mobilities, low-lying energy levels, and their ability to form nanoscale internetworked domains for efficient charge separation [1-4]. However, fullerene electron-acceptor molecules suffer from several drawbacks, such as weak absorption in the visible light region of the solar spectrum, poor tunability in terms of energy level, and morphological instability over time. In recent years, great efforts have been devoted to developing non-fullerene electron acceptors (NFAs), driven by the need to overcome the intrinsic limitations of fullerene acceptors [5-8].

Rapid progress has been made for NFA-based organic photovoltaic (OPV) devices over the past few years: numerous studies reported outstanding power conversion efficiencies (PCEs) of over 17% for single junction OPVs, which far exceeds the PCEs of fullerene-used devices [7,9-12]. This fact demonstrates that NFAs have great potential for future applications in organic solar cells. The reasons for the advanced performance of the NFA-based solar cells are as follows. The energy levels of NFAs can be easily tuned by systematical modification of molecular structures, which allows for achieving a high open circuit voltage ($V_{oc}$) when combined with various choices of well-developed electron-donor materials [13-17]. NFAs have strong near-infrared (IR) light harvesting capability and comprise a complementary broad range light absorption when they are blended with high bandgap polymer donors, which would be beneficial to increasing the short circuit current ($J_{sc}$). In addition, planar NFA molecular backbones increase the intermolecular interactions with an appropriate crystalline domain size in the photoactive layer, enabling efficient charge carrier transport [7],[17-20]. There are also some reports that the morphological stability for NFA-based OPVs is better than that of the fullerene acceptor-based OPVs [21-25].

The relationship between the molecular structure of NFAs and material properties should be understood to properly design an effective electron-acceptor molecule for high-performance organic solar cells. NFAs are typically designed to have a planar structure composed of alternating electron-donor (D) units and electron-acceptor (A) units [13-14,21-24,26-29]. Symmetrical A-D-A or D-A-D backbone structures with well-designed alkyl side chains enable proper self-assembly through intermolecular interactions between the backbone structures or between the alkyl side chains, thereby improving crystallinity and increasing long-range molecular order in thin films. Moreover, the linkage of A or D chemical moieties dictates light absorption and energy level alignment of the highest occupied molecular orbital (HOMO) and the lowest unoccupied molecular orbital (LUMO) levels of the NFAs to polymer donors for high photovoltaic properties. It is also well known that the fluorination of molecular backbones improves OPV device performance due to the following reasons: (i) fluorination simultaneously down-shifts the HOMO and LUMO levels. Thus the molecular bandgap energy remains the same [30-31]; (ii) the

small size of fluorine barely causes steric hindrance; (iii) non-covalent interactions such as F⋯H and F⋯S interactions enhance intramolecular or intermolecular interactions, increasing crystallinity [31-35]; and (iv) fluorinated semiconducting molecules often show higher absorption coefficients compared to their non-fluorinated counterparts [26-27,36].

In this work, we investigated the effect of systematical modifications in the backbone structures or alkyl side chains on NFA material characteristics and photovoltaic properties. As seen in Fig. 1, all molecules were designed by employing intramolecular F⋯H, N⋯H, F⋯S, or N⋯S interactions to ensure the planarity of each molecule [31-35]. The DFD series (the chemical structures of DFDO-RC2 and DFDE-RC2 are shown in Fig. 1(a) and Fig. 1(b)) molecules consist of electron-deficient difluorobenzothiadiazole (F) as a core, electron-rich dithienosilole (D) as a π-conjugated bridge, and benzodiathiazole-connected 3-ethylrhodanine (RC2) units at each end. By employing two types of alkyl chains, octyl (O) and 2-ethylhexyl (E), as alkyl side chains, we intended to study how alkyl side chains affect intermolecular organizations. In the PTB7-Th:DFD-RC2 based OPV devices, the HOMO-HOMO energy offset (≤0.09 eV) between the DFD-RC2 materials and PTB7-Th was insufficient, which resulted in low PCE values (≤1.30%). Thus we replaced difluorobenzothiadiazole (F) with difluorobenzene (FBz)

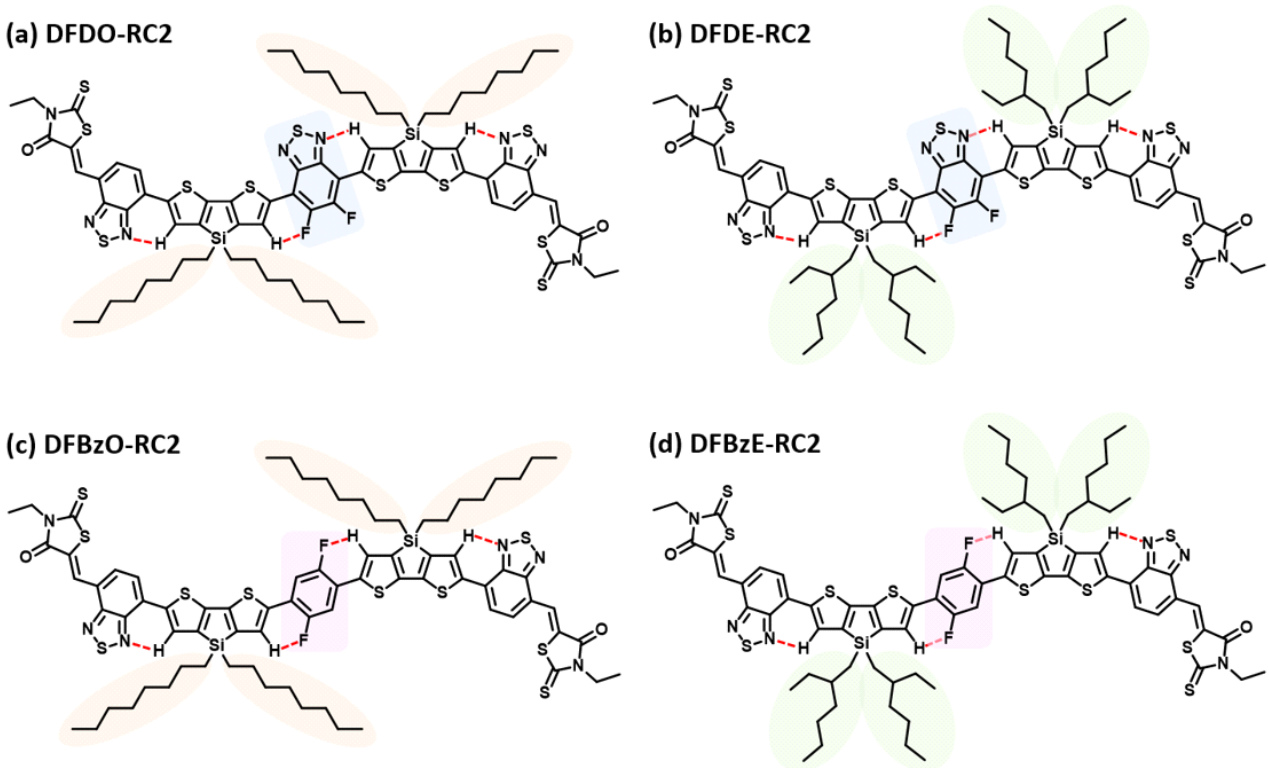


**Fig. 1.** The chemical structures of (a) DFDO-RC2, (b) DFDE-RC2, (c) DFBzO-RC2 and (d) DFBzE-RC2 molecules. (non-covalent intramolecular interactions are shown in dotted red lines).

moiety to achieve enough HOMO-HOMO offset. The resulting DFBz series (the chemical structures of DFBzO-RC2 and DFBzE-RC2 are shown in Fig. 1(c) and Fig. 1(d)) molecules have indeed lowered HOMO levels and thus increased the HOMO-HOMO energy offsets between DFBz-RC2 molecules and PTB7-Th. Moreover, the extinction coefficients and crystallinity of the DFBz series were improved. DFBzE-RC2 exhibited optimal phase separation with PTB7-Th and showed interconnected nanoscale domains, whereas DFBzO-RC2 showed excessive phase separation with PTB7-Th. As a result, the highest $J_{sc}$ and fill factor (FF) values were observed in PTB7- Th:DFBzE-RC2 device. We also note that a remarkably low energy loss of 0.51 eV and high $V_{oc}$ of 1.07 eV was attained in the PTB7-Th:DFBzE-RC2 device.

## 2. RESULTS AND DISCUSSION

The synthesis of NFAs (DFDO-RC2, DFDE-RC2, DFBzO-RC2, and DFBzE-RC2) are summarized in Fig. 2 and Fig. 3. The specific synthesis procedures

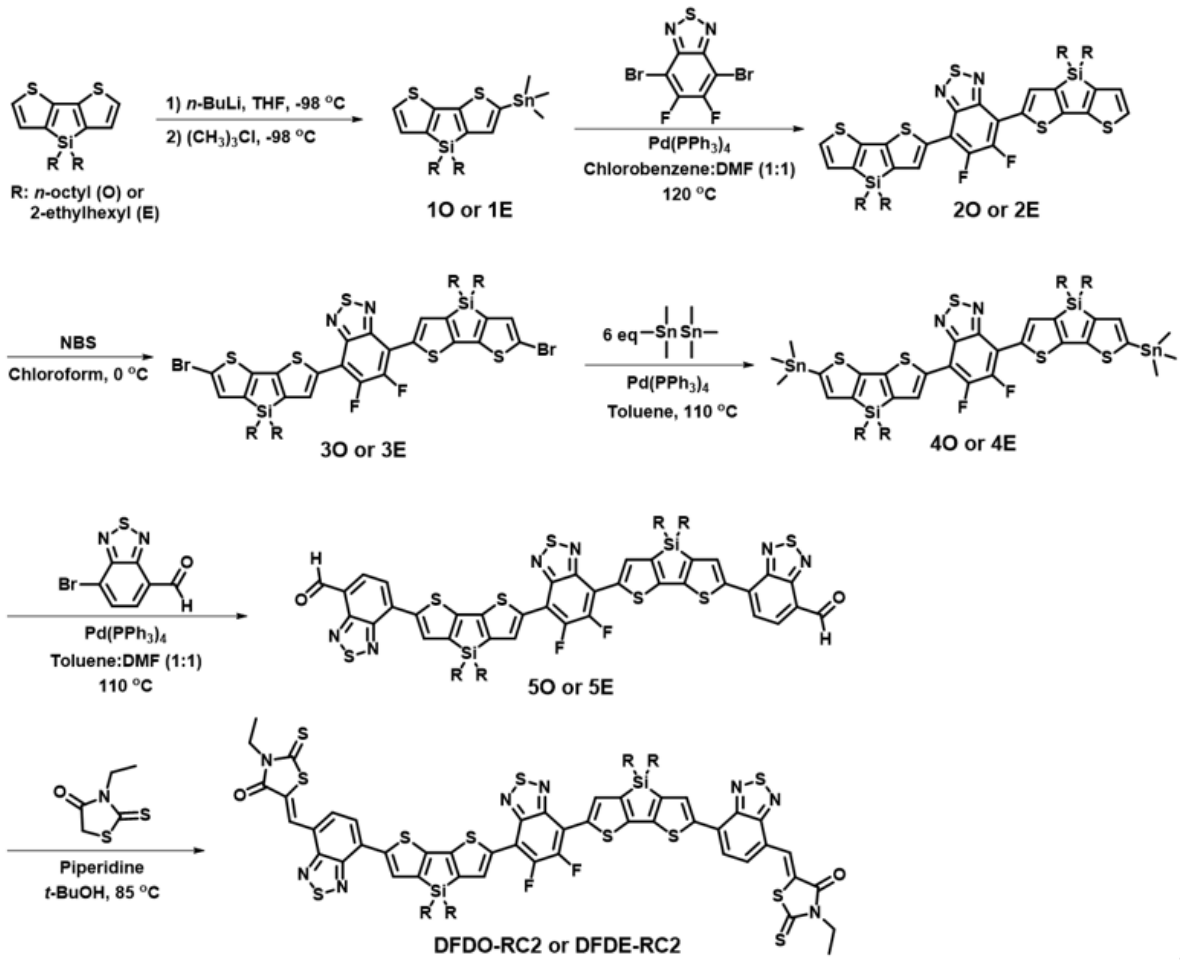


**Fig. 2.** Synthetic routes to DFDO-RC2 and DFDE-RC2.

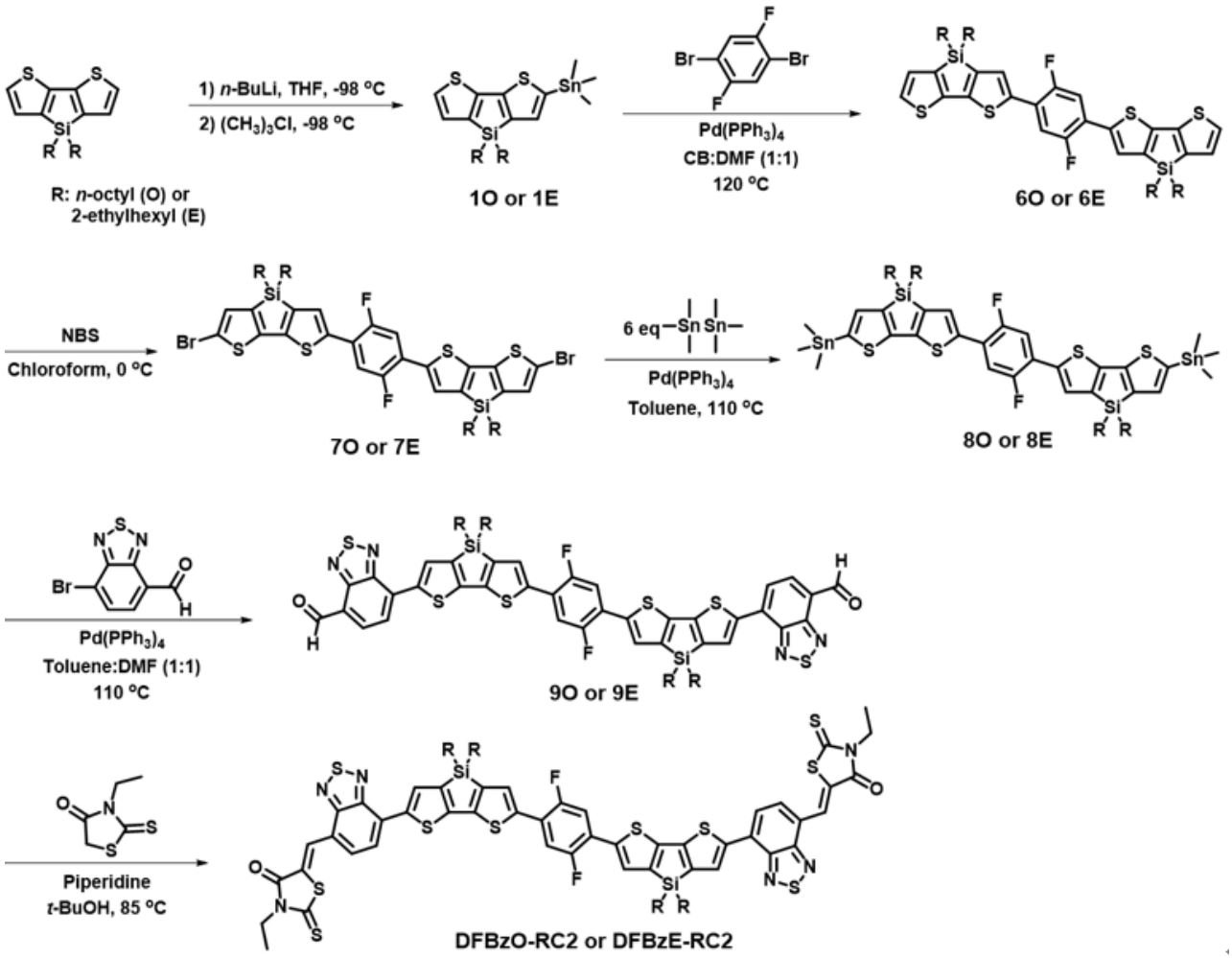


**Fig. 3.** Synthetic routes to DFBzO-RC2 and DFBzE-RC2.

are described in Supplementary Information. Molecules 1O, 1E, 2O, 2E, 3O, and 3E were synthesized according to the literature procedure [34]. Molecules 6O, 6E, 7O, and 7E were synthesized in a similar method. Stille coupling of 3O, 3E, 7O, and 7E with hexamethylditin afforded the 4O, 4E, 8O, and 8E, respectively. 4O, 4E, 8O, and 8E were then each coupled with 7-bromo-2,1,3-benzothiadiazole-4-carboxaldehyde to respectively yield 5O, 5E, 9O, and 9E. Subsequent Knoevenagel condensation of 5O, 5E, 9O, and 9E with 3-ethylrhodanine afforded DFDO-RC2, DFDE-RC2, DFBzO-RC2, and DFBzE-RC2 as final products. The synthesized molecules were characterized by matrix-assist laser desorption ionization time-of-flight mass spectrometry (MALDI-TOF MS) and HNMR (SI Figs. S1-S38)[1]. The synthesized NFAs are soluble in organic solvents such as toluene, chloroform, or chlorobenzene.

Density functional theory (DFT) calculations (B3LYP, 6-311G (d,p)) were carried out to investigate the elec-

tronic structures and molecular geometries of the synthesized NFAs. Fig. 4 displays the front and side views of optimized geometries of the NFAs. DFDO-RC2 and DFDE-RC2 molecules were designed to have planar structures through intramolecular non-covalent and Fig. 1(b)). DFT calculations revealed that the DFD series have highly planar backbones with dihedral angles ranging from 0.10° to 0.74° between difluorobenzothiadiazole moieties and the neighboring dithienosilole groups. The use of difluorinated benzene as a core, which can induce F···H and N···H interactions between fluorine in difluorobenzene and hydro-

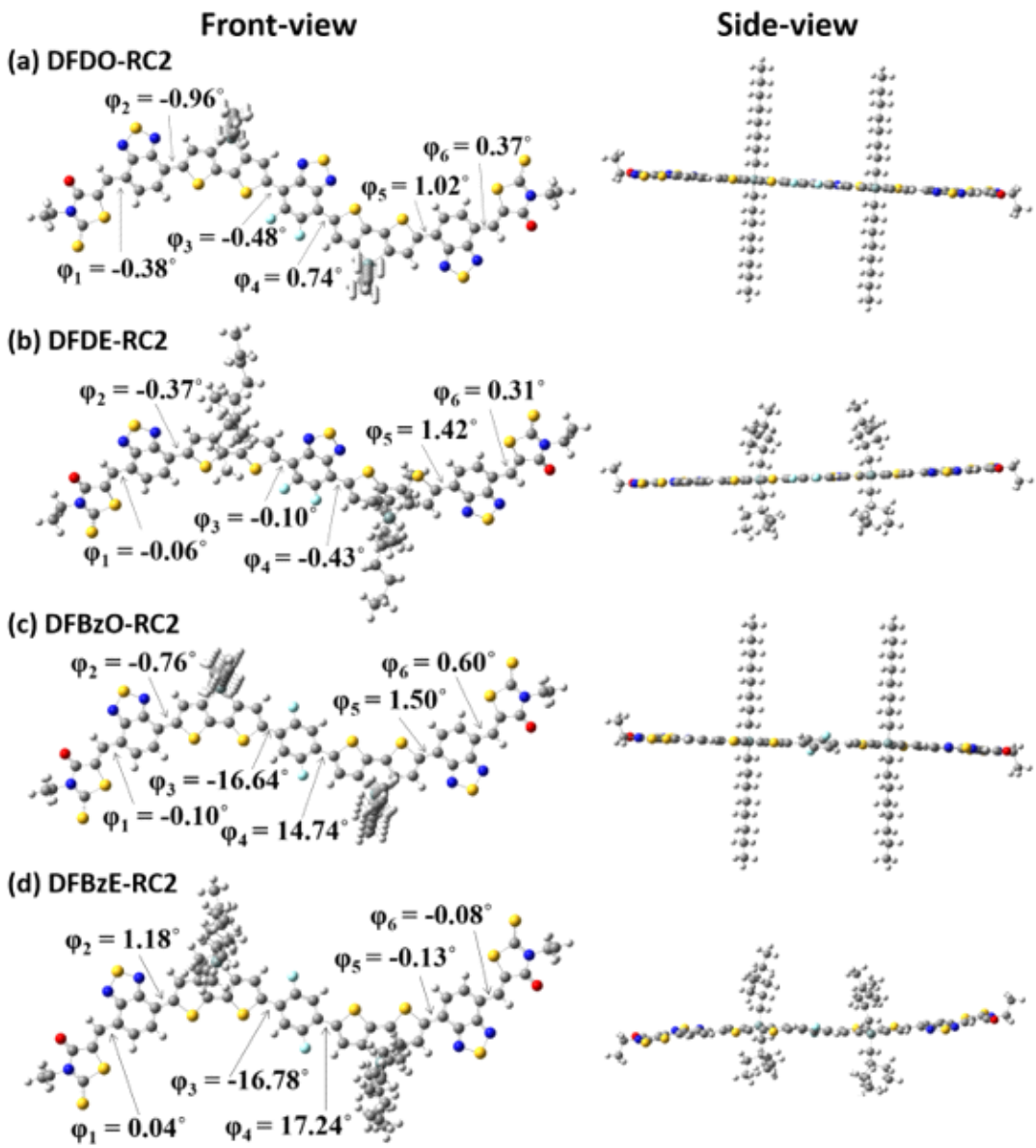


**Fig. 4.** Optimized geometries of the NFAs: (a) DFDO-RC2, (b) DFDE-RC2, (c) DFBzO-RC2, and (d) DFBzE-RC2.

gen in dithienosilole units, also induces the planar backbone in the DFBzO-RC2 and DFBzE-RC2 molecules (Fig. 1(c) and Fig. 1(d)). Optimized DFT calculations of the resulting DFBz series molecules showed dihedral angles ranging from 14.74° to 17.24° (Fig. 4(c) and Fig. 4(d)), which were somewhat increased compared to those of DFD molecules (Fig. 4(a) and Fig. 4(b)), indicating a slightly decreased planarity in an aromatic backbone structure. Although some minor differences were observed in the dihedral angles for DFD and DFBz series, we note that the dihedral angles exhibit values lower than 20°, so all the molecules can have an effective π-conjugation along the molecular backbone. Fig. 5 displays surface plots and energy levels of molecular HOMOs and LUMOs. The HOMO/LUMO levels were −5.323 eV/−3.556 eV for DFDO-RC2 (Fig. 5(a)) and −5.335 eV/−3.562 eV for DFDE-RC2 (Fig. 5(b)). For the DFD series, which exhibited highly planar backbone structures, electrons in both HOMOs and LUMOs were quite evenly delocalized throughout the molecules. For DFBzO-RC2 and DFBzE-RC2, the HOMO/LUMO levels were respectively calculated to be −5.376 eV/−3.461 eV and −5.391 eV/−3.467 eV (Fig. 5(c) and Fig. 5(d)), in

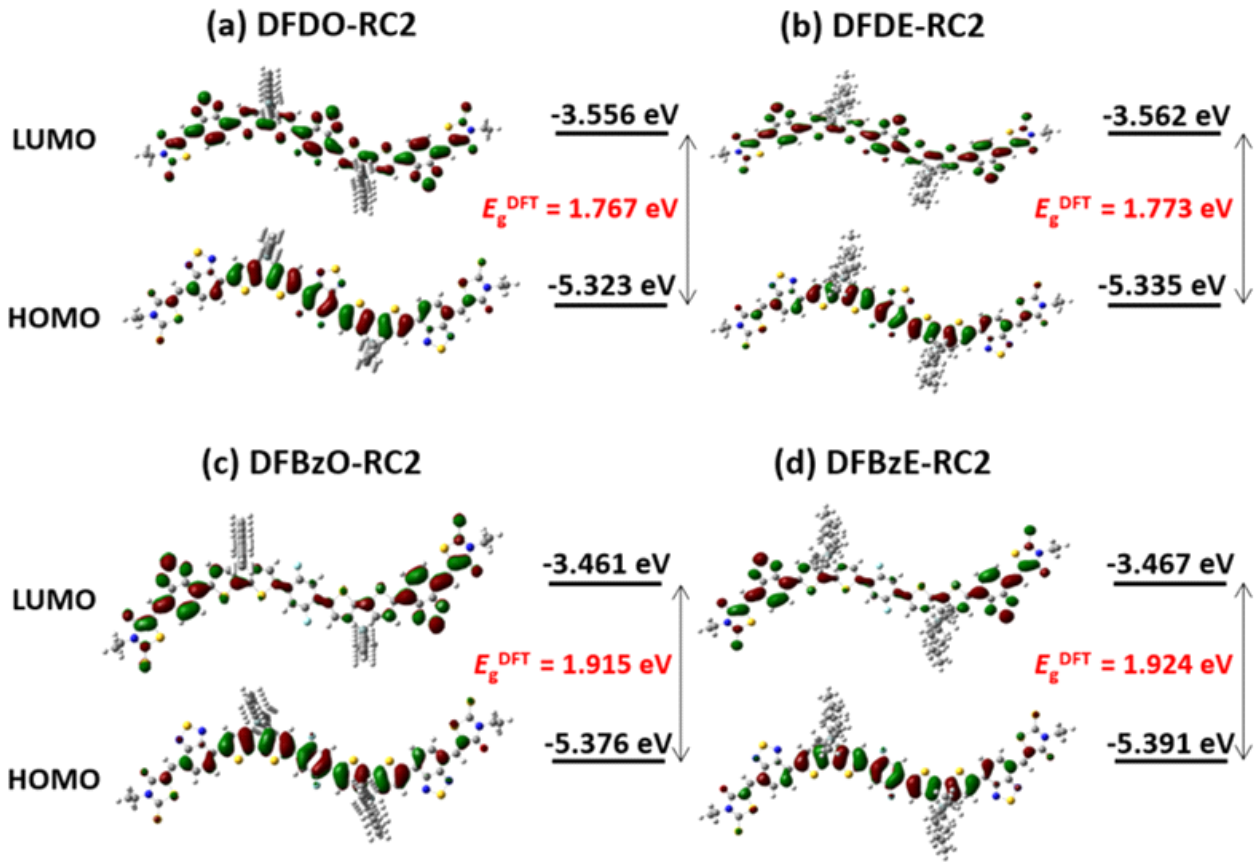


**Fig. 5.** Surface plots and energy levels of molecular HOMOs and LUMOs for (a) DFDO-RC2, (b) DFDE-RC2, (c) DFBzO-RC2, and (d) DFBzE-RC2.

which the HOMO levels were lower, and the LUMO levels were higher than those corresponding values of the DFD series. The HOMOs of the DFBz series are delocalized throughout the molecules, but the LUMOs are more concentrated on the electron-deficient periphery of the molecules. From the HOMO/LUMO levels obtained from DFT results, the bandgaps ($E_g^{DFT}$) were calculated to be 1.767, 1.773, 1.915, and 1.924 eV for DFDO-RC2, DFDE-RC2, DFBzO-RC2, and DFBzE-RC2, respectively.

The electrochemical behaviors of the NFAs were observed through cyclic voltammetry (CV) measurements. The oxidation-reduction cycles of each NFA are drawn in Fig. 6(a)−Fig. 6(d), and an energy diagram in Fig. 6(e) summarizes the molecular energy levels determined by CV (see SI Fig. S39 for cyclic voltammogram of PTB7-Th film). The HOMO and LUMO energy levels were estimated from the onset voltages of oxidation and reduction. The HOMO/LUMO levels of DFDO-RC2 and DFDE-RC2 were −5.20/−3.67 eV and −5.24/−3.71 eV, respectively, which are consistent with the trend observed in the DFT results. DFBzO-RC2 and DFBzE-RC2 showed an equal HOMO level of −5.30 eV, which was lower than the HOMO levels of the DFD series molecules. This observation also agrees well with the DFT results. However, in the case of LUMO levels, CV results revealed that all four molecules exhibited similar LUMO energy values within an experimental error range. At the same time, DFT predicted that the LUMO levels of the DFBz series are higher than those of the DFD series. This observation suggests that the actual molec-

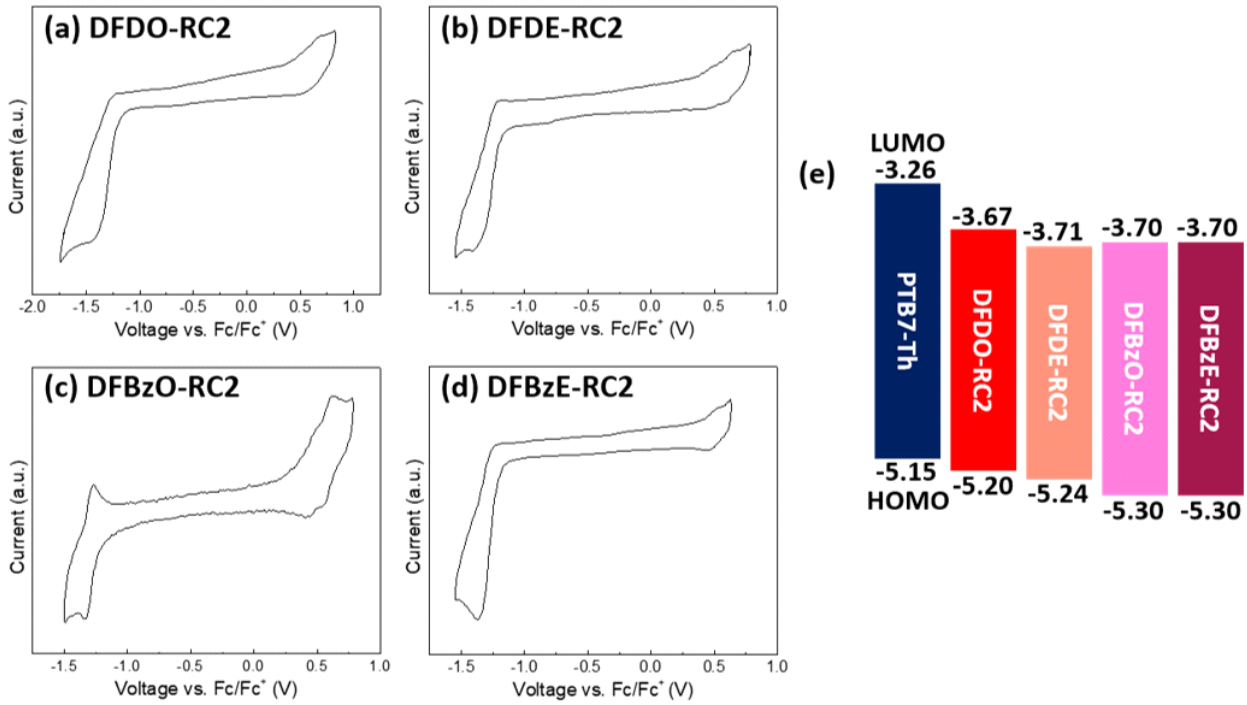


**Fig. 6.** Cyclic voltammograms of (a) DFDO-RC2, (b) DFDE-RC2, (c) DFBzO-RC2, (d) DFBzE-RC2, and (e) an energy level diagram of PTB7-Th and the NFA molecules (unit: eV).

ular backbones of the DFBz series could be more planar than the structures expected from the DFT results so that the π-conjugation between the electron-deficient side-arm units in the molecules would be more effective than expected from the DFT calculations. This fact is supported by the higher crystallinity of DFBz molecules. Importantly, the DFBz molecules showed larger HOMO-HOMO energy offsets with the PTB7-Th electron-donor polymer used in our OPV devices compared to the DFD molecules, which would facilitate effective charge separation at the interface between PTB7-Th and NFAs. All the NFAs exhibited sufficient LUMO-LUMO energy offsets with PTB7-Th, which is beneficial for the efficient separation of excitons formed in the PTB7-Th domains. We also note that there is little difference in LUMO energy levels among the four NFAs, from which we can expect similar $V_{oc}$ values in these NFAs contained OPV devices. From the energy levels obtained from CV, electronic bandgaps ($E_g^{EC}$) of DFDO-RC2, DFDE-RC2, DFBzO-RC2, and DFBzE-RC2 were calculated to be 1.53, 1.53, 1.60, and 1.60 eV, respectively, which is also in good agreement with the trends observed in the DFT results.

Ultraviolet (UV)-visible absorption spectroscopy measurements were carried out to investigate the optoelectronic properties of the NFAs in solution and film states. Two main absorption peaks were observed around 400 and 649 nm for the DFD series and around 414 and 614 nm for the DFBz series in chloroform solution (Fig. 7(a)). The maximum extinction coefficients of the NFAs in solution states were $1.88\times10^4$, $1.94\times10^4$, $2.51\times10^4$, and $2.54\times10^4$ $M^{-1}cm^{-1}$ for DFDO-RC2, DFDE-RC2, DFBzO-RC2, and DFBzE-RC2, respectively. These values are approximately one order of magnitude higher than that ($4.90\times10^3$ $M^{-1}cm^{-1}$) of $PC_{61}BM$ in the solution state [37], demonstrating the potential of these NFAs to yield a greater light absorption than $PC_{61}BM$. Fig. 5(b) displays molecular films of the four NFAs at room temperature (RT). Compared with the absorption in the solution state, all the NFAs displayed significant red-shifts and shoulder peaks in the near IR region, indicating strong intermolecular stacking in the film state. The maximum extinction coefficients of DFDO-RC2, DFDE-RC2, DFBzO-RC2, and DFBzE-RC2 in thin film states were $6.17\times10^4$, $6.33\times10^4$, $8.96\times10^4$, and $8.97\times10^4$ $cm^{-1}$, respectively. Interestingly, the DFBz series molecules showed higher absorption characteristics in the visible light region than those of the DFD series molecules in both solution and thin film states. This feature implies that the DFBz series may yield a greater photocurrent than the DFD series. The DFD molecules showed more red-shifted absorption spectra than the DFBz molecules in both solution and thin film states (Fig. 7(a) and Fig. 7(b)). Thus, smaller optical bandgaps ($E_g^{opt}$: calculated from the onset wavelength in the RT films of the four NFAs) were determined in DFDO-RC2 (1.43 eV) and DFDE-RC2 (1.50 eV) than those of DFBzO-RC2 (1.54 eV) and DFBzE-RC2 (1.58 eV). The optical bandgap tendencies are following electronic bandgaps obtained from the DFT calculations ($E_g^{DFT}$) and the CV measurements ($E_g^{EC}$). NFA films were placed at four temperatures, RT, 100, 150, and 200℃ for 10 min to investigate the effect of thermal annealing on molecular films. The normalized UV-visible absorption spectra of these films are displayed in Fig. 7(c)−Fig. 7(f). DFDO-RC2, DFDE- RC2, and

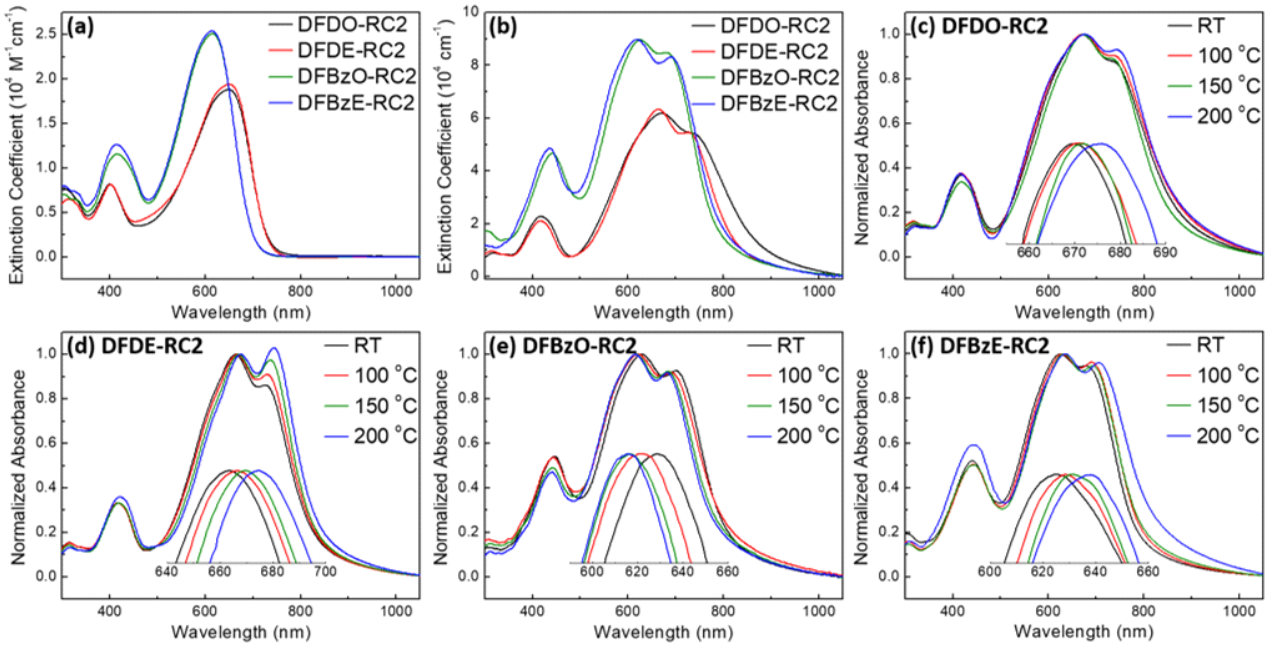


**Fig. 7.** UV-visible absorption spectra of (a) DFDO-RC2, DFDE-RC2, DFBzO-RC2, and DFBzE-RC2 in chloroform solution ($7.0\times10^{-6}$ M). (b) UV-visible absorption spectra of as-cast DFDO-RC2, DFDE-RC2, DFBzO-RC2 and DFBzE-RC2 thin films. UV-visible absorption spectra of NFA thin films annealed at four different temperatures (RT, 100, 150, and 200°C): (c) DFDO-RC2, (d) DFDE-RC2, (e) DFBzO-RC2, and (f) DFBzE-RC2. Zoom-in-spectra of the maximum absorption regions are shown in the insets in Fig. 7(c)–Fig. 7(f).

DFBzE-RC2 films (Fig. 7(c), Fig. 7(d), Fig. 7(f)) showed a bathochromic shift and a pronounced increase of shoulder peaks in the longer wavelength region upon increasing annealing temperatures, a characteristic of *J*-aggregate formation. On the other hand, DFBzO-RC2 (Fig. 7(e)) interestingly exhibited a blue-shift in maximum absorption upon thermal annealing, indicating the *H*-aggregate formation between DFBzO-RC2 molecules [38].

The thermal properties of small molecules were examined by differential scanning calorimetry (DSC). From the DSC curves (Fig. 8(a)∼Fig. 8(d)), melting temperatures ($T_m$) and crystallization temperatures ($T_c$) were determined, which data are summarized in Table 1. For both the DFD and DFBz series molecules, the molecules with 2-ethylhexyl side chains on dithienosilole revealed higher melting points than the corresponding molecules with octyl chains: DFDE-RC2 ($T_m$=320.4℃) DFDO-RC2 ($T_m$=288.4, 293.9℃) and DFBzE-RC2 ($T_m$=276.2℃) DFBzO-RC2 ($T_m$=259.9℃). This melting point difference can be explained by comparing coherence length ($L_c$) from Grazing-Incidence Wide-Angle X-ray Scattering (GIWAXS) results; DFDE-RC2 and DFBzE-RC2 revealed larger crystal sizes compared to DFDO-RC2 and DFBzO-RC2 compounds, which possibly led to greater $T_m$ values. Notably, the molecules with linear octyl side chains exhibited more various thermal transitions than molecules with branched 2-ethylhexyl side chains. DFDO-RC2 (Fig. 8(a) showed two melting peaks at 288.4℃ and 293.9℃, and DFBzO-

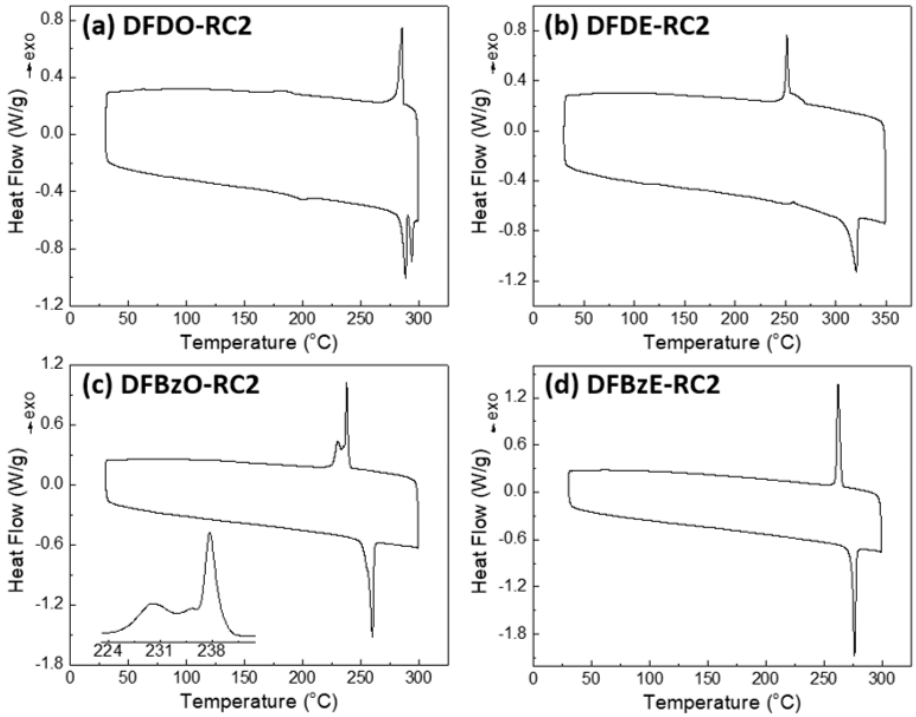


**Fig. 8.** DSC thermograms of (a) DFDO-RC2, (b) DFDE-RC2, (c) DFBzO-RC2, and (d) DFBzE-RC2, measured at a temperature scan rate of 10°C/min.

**Table 1.** Optoelectronic and thermal properties of DFDO-RC2, DFDE-RC2, DFBzO-RC2, and DFBzE-RC2

| Molecule | Absorption wavelength (nm) | | | $E_g^{opt.}$ (eV)[b] | $E_g^{EC}$ (eV)[c] | HOMO (eV)[c] | LUMO (eV)[c] | $\varepsilon$ ($10^4$ $M^{-1}cm^{-1}$)[a] | $\varepsilon$ ($10^4$ $cm^{-1}$)[b] | $T_m$ (°C)[d] | $T_c$ (°C)[d] |
|---|---|---|---|---|---|---|---|---|---|---|---|
| | $\lambda_{max}$ solution[a] | $\lambda_{max}$ film[b] | $\lambda_{onset}$ film[b] | | | | | | | | |
| DFDO-RC2 | 400, 648 | 417, 668 | 865 | 1.43 | 1.53 | −5.20 | −3.67 | 1.88 | 6.17 | 288.4, 293.9 | 285.6 |
| DFDE-RC2 | 400, 650 | 415, 662 | 825 | 1.50 | 1.53 | −5.24 | −3.71 | 1.94 | 6.33 | 320.4 | 251.7 |
| DFBzO-RC2 | 414, 615 | 443, 619 | 807 | 1.54 | 1.60 | −5.30 | −3.70 | 2.51 | 8.96 | 259.9 | 237.7, 235.3, 230.0 |
| DFBzE-RC2 | 414, 613 | 441, 625 | 786 | 1.58 | 1.60 | −5.30 | −3.70 | 2.54 | 8.97 | 276.2 | 262.1 |

[a]Measured from chloroform solution at a concentration of $7.0\times10^{-6}$ M.
[b]Measured from thin films that were spin-coated from 5 mg/mL chloroform solution.
[c]Cyclic voltammetry was performed with 0.1 M tetrabutylammonium hexafluorophosphate in dichloromethane.
[d]Determined by differential scanning calorimetry at a temperature scan rate of 10°C/min.

RC2 (Fig. 8(c)) showed three crystallization temperatures of 237.7℃, 235.3℃, and 230.0℃, which suggests that liquid crystalline state might exist in these two molecules having octyl side chains [39].

GIWAXS patterns of the molecular thin films were obtained to examine the effect of thermal annealing on the crystallinity and long-range ordering of the NFAs. The GIWAXS images of NFA films annealed at RT, 100℃, 150℃, and 200℃ are shown in Fig. 9(a)-Fig. 9(d), and the GIWAXS parameters are summarized in Table 2. The line-cut profiles of films are shown in SI Fig. S40-S44. The out-of-plane profiles were drawn from the $q_z$ direction signal at $q_y$=0.00 Å$^{-1}$, and the in-plane profiles were extracted from the $q_y$ direction signal at $q_z$=0.03 Å$^{-1}$. In all the molecular films, enhanced long-range ordering of the NFAs in the $q_z$ di-

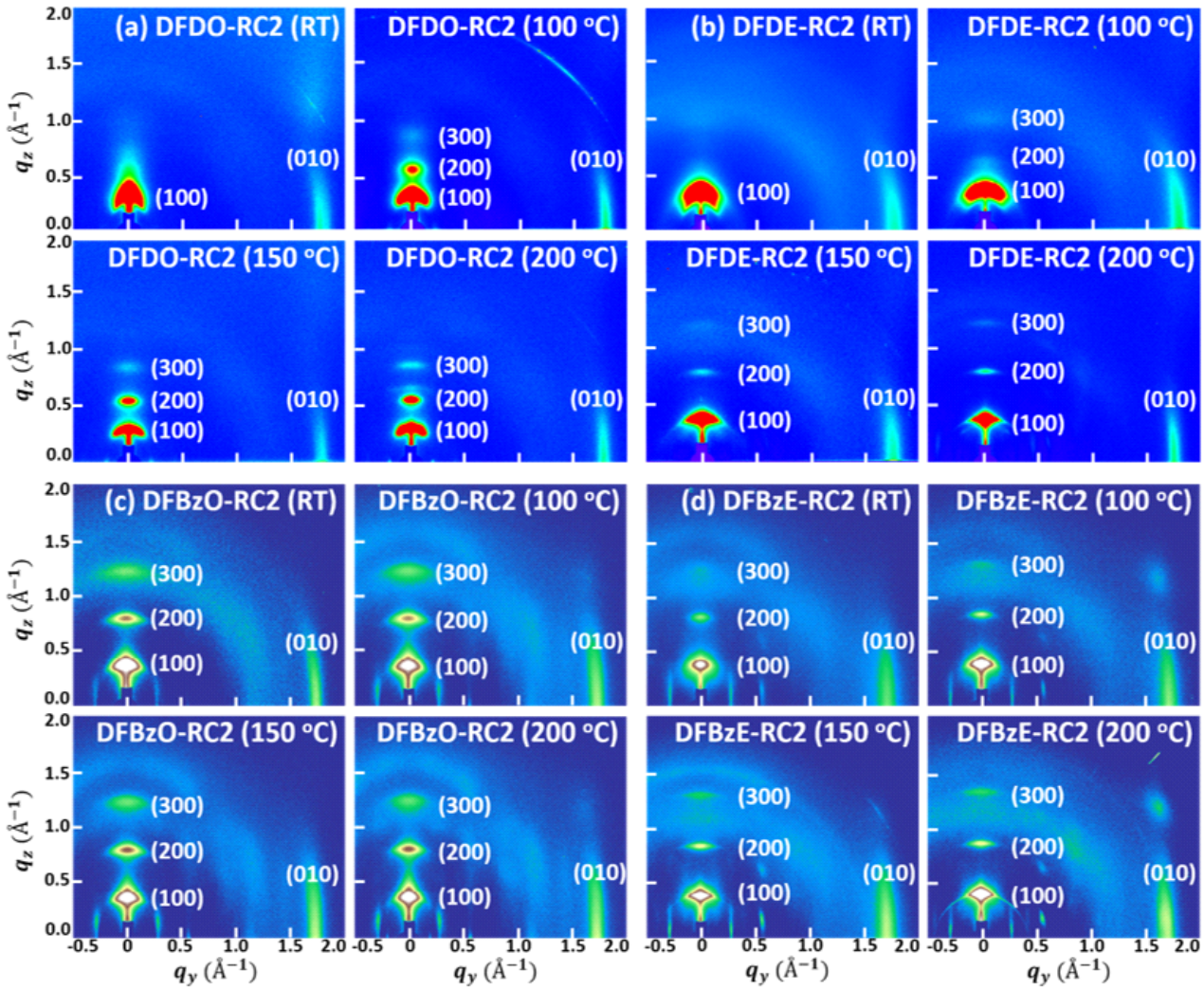


**Fig. 9.** GIWAXS images of (a) DFDO-RC2, (b) DFDE-RC2, (c) DFBzO-RC2, and (d) DFBzE-RC2 thin films annealed at RT, 100, 150, and 200°C.

**Table 2.** Summary of GIWAXS parameters of DFDO-RC2, DFDE-RC2, DFBzO-RC2, and DFBzE-RC2

| Material | Temperature (℃) | Lamellar spacing from (100) in the $q_z$ direction | | | | π-π spacing from (010) in the $q_y$ direction | | | |
|---|---|---|---|---|---|---|---|---|---|
| | | $q_{(100)}$ (Å$^{-1}$) | FWHM (Å$^{-1}$1) | $d$ (Å) | $L_c$ (nm) | $q_{(010)}$ (Å$^{-1}$) | FWHM (Å$^{-1}$) | $d$ (Å) | $L_c$ (nm) |
| DFDO-RC2 | RT | 0.396 | 0.1092 | 15.884 | 5.181 | 1.775 | 0.1012 | 3.539 | 5.586 |
| | 100 | 0.308 | 0.0557 | 20.392 | 10.155 | 1.783 | 0.0829 | 3.524 | 6.821 |
| | 150 | 0.321 | 0.0433 | 19.598 | 13.058 | 1.781 | 0.0833 | 3.527 | 6.791 |
| | 200 | 0.330 | 0.0375 | 19.050 | 15.094 | 1.772 | 0.0792 | 3.545 | 7.139 |
| DFDE-RC2 | RT | 0.445 | 0.0807 | 14.125 | 7.005 | 1.781 | 0.1184 | 3.527 | 4.776 |
| | 100 | 0.426 | 0.0567 | 14.753 | 9.970 | 1.784 | 0.1203 | 3.521 | 4.700 |
| | 150 | 0.458 | 0.0357 | 13.710 | 15.843 | 1.784 | 0.1224 | 3.521 | 4.620 |
| | 200 | 0.473 | 0.0229 | 13.288 | 24.687 | 1.743 | 0.0806 | 3.604 | 7.015 |
| DFBzO-RC2 | RT | 0.426 | 0.0420 | 14.760 | 13.464 | 1.774 | 0.1072 | 3.543 | 5.273 |
| | 100 | 0.427 | 0.0378 | 14.706 | 14.964 | 1.766 | 0.0766 | 3.558 | 7.386 |
| | 150 | 0.433 | 0.0360 | 14.502 | 15.708 | 1.760 | 0.0770 | 3.569 | 7.345 |
| | 200 | 0.437 | 0.0340 | 14.375 | 16.632 | 1.759 | 0.0736 | 3.572 | 7.683 |
| DFBzE-RC2 | RT | 0.446 | 0.0200 | 14.076 | 28.274 | 1.747 | 0.1072 | 3.598 | 5.273 |
| | 100 | 0.460 | 0.0240 | 13.667 | 23.562 | 1.755 | 0.1102 | 3.580 | 5.132 |
| | 150 | 0.469 | 0.0200 | 13.386 | 28.274 | 1.746 | 0.1028 | 3.599 | 5.502 |
| | 200 | 0.475 | 0.0260 | 13.238 | 21.749 | 1.740 | 0.1208 | 3.612 | 4.682 |

rection was observed upon thermal annealing; that is, the peaks associated with lamellar stacking of the NFAs became stronger. As-cast DFDO-RC2 (Fig. 9(a)) and DFDE-RC2 films (Fig. 9(b)) exhibited only (100) peaks in the out-of-plane direction, and 100, 150, and 200℃ - annealed films exhibited high order (200), and (300) peaks as well. For DFBzO-RC2 films (Fig. 9(c)) and DFBzE-RC2 films (Fig. 9(d)), (100), (200), and (300) peaks appeared even in the as-cast films, which means that the DFBz series molecular films are more crystalline than the DFD series molecular films and became more prominent upon thermal annealing. From the comparison of (100) peaks of the NFAs, it is found that the backbone structure of the DFBz series facilitates molecular packing better; the (100) peak of DFDO-RC2 appeared at $q_z$=0.396 Å$^{-1}$ ($d$=15.884 Å), and the (100) peak of DFBzO-RC2 showed at $q_z$=0.426 Å$^{-1}$ ($d$=14.760 Å), which indicates that octyl chains in DFBzO-RC2 are more closely interdigitated, thus showing more closely packed lamellar structure compared to DFDO-RC2. A similar feature was found between DFDE-RC2 and DFBzE-RC2. These results suggest that the molecular backbone of the DFBz series in film state could be more planar than the struc-

ture observed in the DFT results. The (200) and (300) peaks were more prominent in 100, 150, and 200℃ films of DFDO-RC2 than in DFDE-RC2 films (Fig. 9(a) and Fig. 9(b)). For all the NFA films, (010) peaks were observed in the in-plane direction, indicating that all the NFAs tend to adopt an edge-on orientation mainly. In as-cast molecular films, the π-π stacking peak position and the corresponding d spacing values of each molecule are as follows: DFDO-RC2 ($q_y$= 1.775 Å$^{-1}$ ($d$=3.539 Å)), DFDE-RC2 ($q_y$=1.781 Å$^{-1}$ ($d$=3.527 Å)), DFBzO-RC2 ($q_y$=1.774 Å$^{-1}$ ($d$=3.543 Å)), and DFBzE-RC2 ($q_y$=1.747 Å$^{-1}$ ($d$=3.598 Å)). DFDO-RC2 and DFDE-RC2 had slightly more closely packed π-π stacking structures than DFBzO-RC2 and DFBzE-RC2. The closed π-π stacking may be associated with the fact that the maximum absorption peak in the UV is more red-shifted in the DFD series than the DFBz series when going from the solution state to the film state (Fig. 5(a) and Fig. 5(b)). These facts may be attributed to the characteristic of the more heteroatom-contained planar difluorobenzothiadiazole moiety, which gives rise to strong intramolecular interactions with planar structure compared to a simpler difluorobenzene moiety. According to the coherence length values in the $q_z$ direction, the relatively larger crystal sizes of DFDE-RC2 and DFBzE-RC2 were observed compared to DFDO-RC2 and DFBzO-RC2. This fact is in accordance with UV-visible absorption spectral features (Fig. 7(b)); molecules with 2-ethylhexyl as side chains showed more prominent absorption changes upon thermal annealing than the corresponding molecules with octyl side chains. This result is because the shorter alkyl chain length of 2-ethylhexyl chains may have enhanced the molecular stacking in DFDE-RC2 and DFBzE-RC2 molecules [40].

### 2.1. Photovoltaic Properties

OPV devices were fabricated with the inverted type architecture: glass/ITO/ZnO/PEIE/PTB7-Th:NFA/$V_2O_5$/Ag. *J-V* curves and external quantum efficiency (EQE) spectra of optimized OPV devices are shown in Fig. 10(a) and Fig. 10(b), and their photovoltaic performance parameters are summarized in Table 3. PTB7-Th:DFBz devices yielded outstanding open-circuit vol-

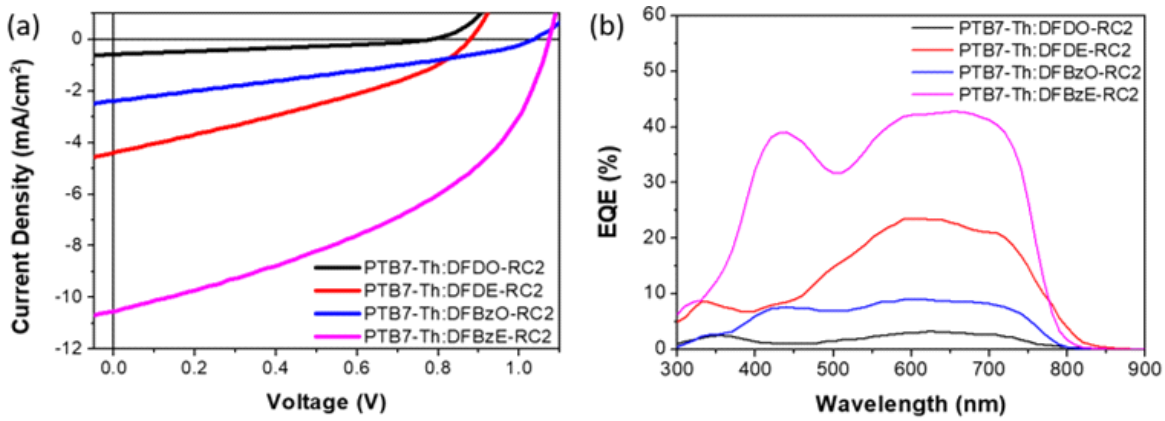


**Fig. 10.** (a) J–V characteristics and (b) EQE spectra of inverted type organic solar cells based on the four devices: PTB7-Th:DFDO-RC2, PTB7-Th:DFDE-RC2, PTB7-Th:DFBzO-RC2, and PTB7-Th:DFBzE-RC2.

**Table 3.** Photovoltaic performance parameters of optimized organic solar cells based on PTB7-Th:NFA active layers

| Devices | $V_{oc}$ (V) | $E_{loss}$ (eV)[a] | $J_{sc}$ (mA/cm$^2$) | FF | PCE$_{max}$ (%) |
|---|---|---|---|---|---|
| PTB7-Th:DFDO-RC2 | 0.78 (0.76±0.03) | 0.65 | 0.58 (0.56±0.04) | 0.34 (0.33±0.02) | 0.15 (0.14±0.02) |
| PTB7-Th:DFDE-RC2 | 0.88 (0.87±0.01) | 0.62 | 4.39 (4.39±0.05) | 0.34 (0.33±0.01) | 1.30 (1.71±0.03) |
| PTB7-Th:DFBzO-RC2 | 1.03 (1.03±0.01) | 0.51 | 2.38 (2.35±0.06) | 0.30 (0.29±0.01) | 0.75 (0.71±0.04) |
| PTB7-Th:DFBzE-RC2 | 1.07 (1.070±0.001) | 0.51 | 10.53 (10.06±0.38) | 0.43 (0.42±0.01) | 4.85 (4.52±0.29) |

[a]Energy loss was calculated from the equation $E_{loss}= E_g^{NFA}-eV_{oc}$.

tages of over 1 V, while PTB7-Th:DFDO-RC2 and PTB7-Th:DFDE-RC2 devices exhibited relatively lower $V_{oc}$ values of 0.88 V and 0.78 V, respectively. Higher $V_{oc}$ values were obtained in PTB7-Th:DFBz devices due to the relatively low energy loss ($E_{loss}$) of 0.51 eV in the PTB7-Th:DFBzO-RC2 and PTB7-Th:DFBzE-RC2 devices. This low $E_{loss}$ value is comparable to that of inorganic solar cells [41-42], and also is among the lowest value achieved in NFA-based polymer solar cells reported so far [13],[43-47]. The energy loss was calculated from the $E_{loss}$=E$_g^{NFA}$-e$V_{oc}$ equation where $E_g$ corresponds to the optical bandgap of the NFAs [13,48-49]. A higher short-circuit current ($J_{sc}$) of 4.39 mA/cm$^2$ was obtained from PTB7-Th :DFDE-RC2 devices, compared with 0.58 mA/cm$^2$ for PTB7-Th:DFDO-RC2 devices. The high $J_{sc}$ can be explained by the fact that DFDE-RC2 has a greater HOMO-HOMO energy offset with PTB7-Th and a finer surface morphology than DFDO-RC2 (see below the morphology study). Relative to the DFD series, higher $J_{sc}$ values (2.38 mA/cm$^2$ for PTB7-Th: DFBzO-RC2 devices and 10.53 mA/cm$^2$ for PTB7-Th: DFBzE-RC2 devices) were obtained in DFBz series. Higher photocurrent density in the DFBz series can be accounted for by the larger HOMO-HOMO energy offset with PTB7-Th than the DFD series. In addition, the DFBz series has higher extinction coefficients than the DFD series. Among the DFBz series, PTB7-Th: DFBzO-RC2 blend film revealed a rough morphology with large aggregates, while PTB7-Th:DFBz-RC2 blend film had the ideal morphology among the four PTB7-Th:NFA blend films which can be accounted for the highest $J_{sc}$ and FF values for PTB7-Th:DFBz-RC2 devices (see below the morphology study). As a result, the highest efficiency of 4.85% was obtained from the PTB7-Th:DFBzE-RC2 device, where the three photovoltaic performance parameters, $V_{oc}$, $J_{sc}$, and FF were the highest. EQE measurements were performed to confirm the $J_{sc}$s of the devices. The integrated current densities were calculated to be 0.57 (PTB7-Th:DFDO-RC2), 4.61 (PTB7-Th:DFDE-RC2), 1.92 (PTB7-Th: DFBzO-RC2), and 9.31 mA/cm$^2$ (PTB7-Th:DFBzE-RC2), which were in good agreement with the measured $J_{sc}$ values.

### 2.2. Morphology Study on the Blend Films

Transmission electron microscopy (TEM) images of the PTB7-Th:NFA blend films were obtained to investigate the fibril structures in the blend films (Fig. 11(a) −Fig. 11(d)). If the domain size is too large, geminal recombination occurs before the exciton reaches the electron-donor/electron-acceptor interface, and if the domain size is too small, the chance of bimolecular recombination increases. Therefore, phase separation at an appropriate length scale is important for the parameters of $J_{sc}$ and FF. Large branch-like aggregations were observed in PTB7-Th:DFBzO-RC2 film (Fig. 11(c)), whereas the other three blend films showed phase separation at the nanoscale (Fig. 11(a), Fig. 11(b), Fig. 11(d)). The large aggregation resulted in the low $J_{sc}$ and FF obtained from the PTB7-Th:DFBzO-RC2 device.

In addition, surface morphologies of the PTB7-Th:NFA blend films were examined using atomic force microscopy (AFM) under non-contact mode (Fig. 11(e)−Fig. 11(h)). The root mean square (RMS) values of PTB7-Th:DFDO-RC2, PTB7-Th:DFDE-RC2, PTB7-Th:DFBzO-RC2, and PTB7-Th:DFBzE-RC2 films were 2.37, 1.20, 5.70, and 1.60 nm, respectively. PTB7-Th:DFBzO-RC2 exhibited large-sized grains (Fig. 11(g)), which agrees well with images obtained from TEM. Among the three blend films that showed nanosized fibrillar structure in TEM, relatively rough morphology was observed in PTB7-Th:DFDO-RC2 blend film (Fig. 9(e)). It appears that the electron-donor and electron-acceptor domains are clustered together, in which recombination occurs before the resulting electrons and holes generated in each domain reach the electrodes. PTB7-Th:DFDE-RC2 and PTB7-Th:DFBzE-RC2 blend

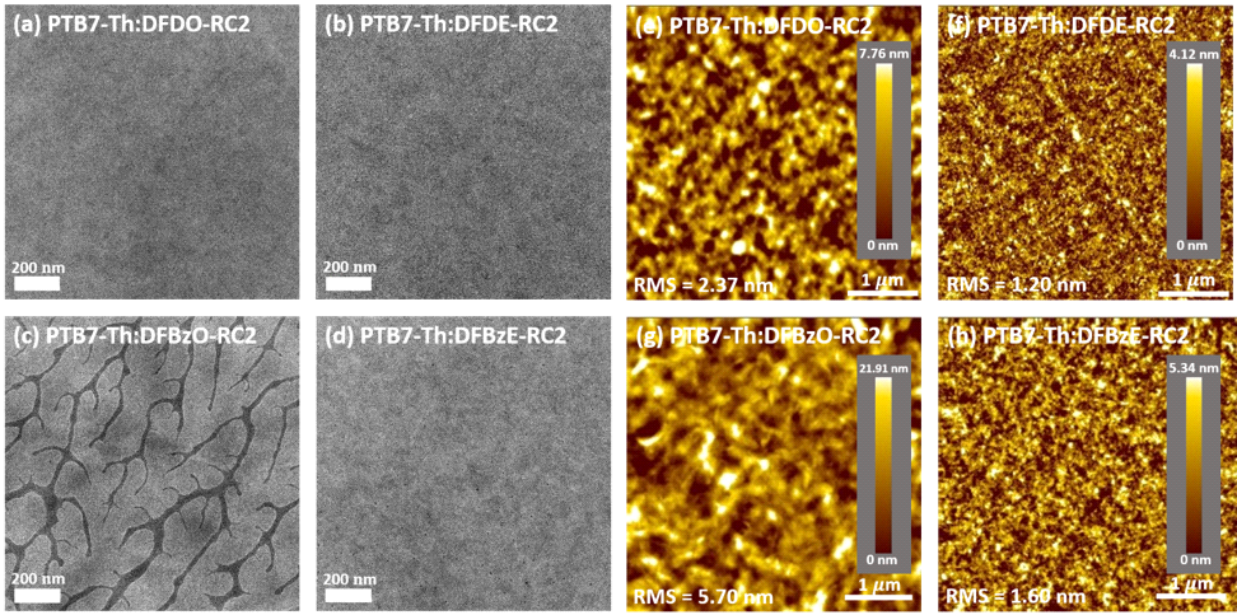


**Fig. 11.** TEM images of (a) PTB7-Th:DFDO-RC2, (b) PTB7-Th:DFDE-RC2, (c) PTB7-Th:DFBzO-RC2, and (d) PTB7-Th:DFBzE-RC2 blend films. Topographic images of (e) PTB7-Th:DFDO-RC2, (f) PTB7-Th:DFDE-RC2, (g) PTB7-Th:DFBzO-RC2, and (h) PTB7-Th:DFBzE-RC2 blend films.

films showed relatively smooth surface morphology. PTB7-Th:DFDE-RC2 exhibited a too fine surface feature (Fig. 11(f)), which induces bimolecular recombination, while PTB7-Th:DFBzE-RC2 exhibited a moderately smooth surface with nanoscale domains (Fig. 11(d) and Fig. 11(h)). Therefore, the highest $J_{sc}$ and FF were obtained in the PTB7-Th:DFBzE-RC2 device containing the ideal morphology among the four blend films.

### 2.3. Grazing-Incidence Wide-Angle X-ray Scattering of Blend Films

GIWAXS measurements were conducted on the PTB7-Th:NFA blend films to investigate the formation of pure electron-donor and electron-acceptor domains in the blend films. The images of PTB7-Th:DFDO-RC2, PTB7-Th:DFDE-RC2, PTB7-Th:DFBzO-RC2, and PTB7-Th:DFBzE-RC2 blend films are shown in Fig. 12(a)−Fig. 12(d), and the GIWAXS parameters of the four blend films are summarized in Table 4. The line-cut profiles in the $q_z$ and $q_y$ directions of the blend films are shown in SI Figs. S45, S46. The blend films were compared with their corresponding molecular films. All the blend films showed more reduced crystallinity, indicating that less ordered phases were formed by blending NFA molecules with PTB7-Th, compared to their molecule-only film counterparts. Nevertheless, the crystalline features of NFAs were maintained to some degree in PTB7-Th:DFDO-RC2 (Fig. 12(a)) and PTB7-Th:DFBzO-RC2 (Fig. 12(c))

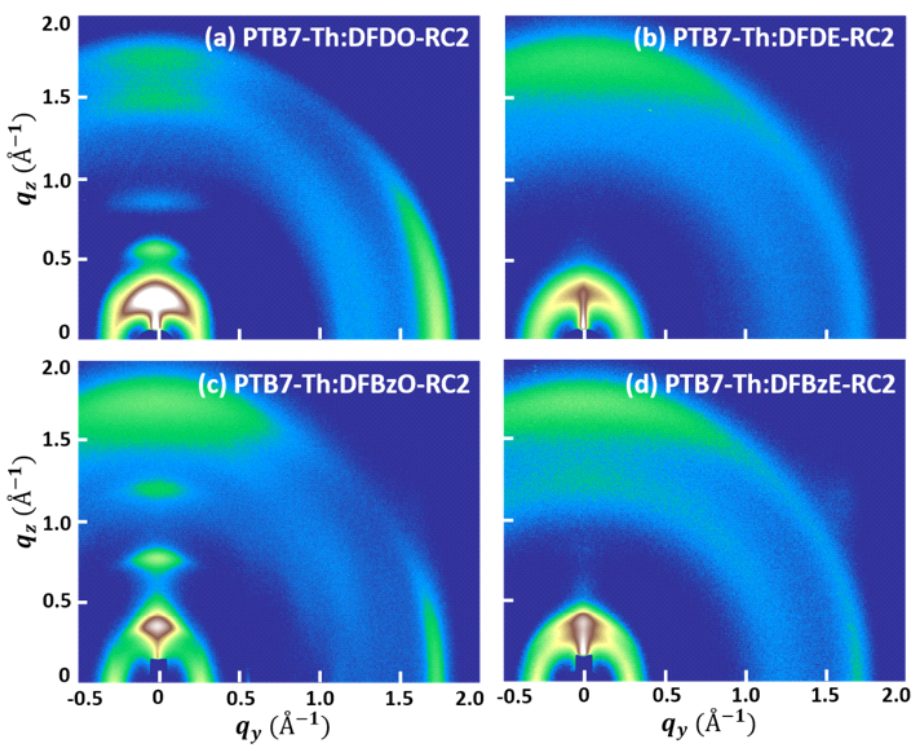


**Fig. 12.** GIWAXS images of (a) PTB7-Th:DFDO-RC2, (b) PTB7-Th:DFDE-RC2, (c) PTB7-Th:DFBzO-RC2, and (d) PTB7-Th:DFBzE-RC2 blend films.

**Table 4.** Summary of GIWAXS parameters of PTB7-Th:DFDO-RC2, PTB7-Th:DFDE-RC2, PTB7-Th:DFBzO-RC2, PTB7-Th:DFBzE-RC2 blend films and PTB7-Th film

| Material | Peak information from the $q_z$ direction | | | | Peak information from the $q_y$ direction | | | |
|---|---|---|---|---|---|---|---|---|
| | $q$ (Å$^{-1}$) | FWHM (Å$^{-1}$) | $D$ (Å) | $L_c$ (nm) | $q$ (Å$^{-1}$) | FWHM (Å$^{-1}$) | $d$ (Å) | $L_c$ (nm) |
| PTB7-Th:DFDO-RC2 | 0.316 | 0.0411 | 19.859 | 13.773 | 1.770 | 0.115 | 3.549 | 4.933 |
| | 0.624 | 0.0571 | 10.076 | 9.903 | | | | |
| | 0.931 | 0.0917 | 6.751 | 6.166 | | | | |
| | 1.508 | 0.213 | 4.167 | 2.657 | | | | |
| | 1.753 | 0.165 | 3.585 | 3.427 | | | | |
| PTB7-Th:DFDE-RC2 | 0.333 | 0.0764 | 18.870 | 7.398 | 1.712 | 0.144 | 3.670 | 3.935 |
| | 1.667 | 0.257 | 3.770 | 2.197 | | | | |
| PTB7-Th:DFBzO-RC2 | 0.422 | 0.0448 | 14.883 | 12.636 | 1.766 | 0.0818 | 3.558 | 6.916 |
| | 0.840 | 0.0697 | 7.483 | 8.108 | | | | |
| | 1.242 | 0.236 | 5.061 | 2.397 | | | | |
| | 1.717 | 0.401 | 3.660 | 1.409 | | | | |
| PTB7-Th:DFBzE-RC2 | 0.419 | 0.0760 | 14.981 | 7.441 | 1.724 | 0.147 | 3.644 | 3.856 |
| | 1.300 | 0.420 | 4.833 | 1.348 | | | | |
| | 1.730 | 0.192 | 3.631 | 2.948 | | | | |
| PTB7-Th | 1.591 | 0.382 | 3.948 | 1.481 | 0.262 | 0.0976 | 23.997 | 5.793 |
| | | | | | 1.647 | 0.221 | 3.816 | 2.554 |

films. In PTB7-Th:DFDO-RC2 film, (100) peak coming from DFDO-RC2 and PTB7-Th (see SI Fig. S47 for GIWAXS data of PTB7-Th film) were observed at $q_z$=0.316 Å$^{-1}$ ($d$=19.859 Å), and (200) and (300) peaks coming from DFDO-RC2 appeared at $q_z$=0.624 Å$^{-1}$ and $q_z$=0.931 Å-1, respectively. The π-π stacking structure in PTB7-Th:DFDO-RC2 film was observed at $q_y$=1.770 Å$^{-1}$ ($d$=3.549 Å). The characteristic (010) peak of PTB7-Th ($q_z$=1.591 Å$^{-1}$, $d$=3.948 Å) was not well observed in PTB7-Th:DFDO-RC2 film, indicating that PTB7-Th and DFDO-RC2 are mixed. In PTB7-Th:DFBzO-RC2 film, (100) peak coming from DFBzO-RC2 and PTB7-Th were observed at $q_z$=0.422 Å$^{-1}$ ($d$=14.883 Å), and very strong (200) and (300) peaks coming from DFBzO-RC2 respectively appeared at $q_z$=0.840 Å$^{-1}$ and qz=1.242 Å$^{-1}$. Also, the π-π stacking structure of DFBzO-RC2 was observed at $q_y$=1.766 Å$^{-1}$ ($d$=3.558 Å), and a peak indicating the face-on domains of PTB7-Th was observed at $q_z$=1.717 Å$^{-1}$ ($d$=3.660 Å). That is, in PTB7-Th:DFBzO-RC2 blend film, the phase separation between PTB7-Th and DFBzO-RC2 was more prominent compared to PTB7-Th:DFDO-RC2 blend film. PTB7-Th:DFDE-RC2 and PTB7-Th:DFBzE-RC2 blend films showed a more

amorphous-like feature relative to PTB7-Th: DFDO-RC2 and PTB7-Th:DFBzO-RC2 blend films. In PTB7-Th:DFDE-RC2 film, (100) peak coming from DFDE-RC2 and PTB7-Th appeared at $q_z$=0.333 Å$^{-1}$ ($d$= 18.870 Å), π-π interaction peak was observed at $q_z$= 1.667 Å$^{-1}$ ($d$=3.770 Å). This observation agrees with the too well-mixed phase observed in the AFM image of PTB7-Th:DFDE-RC2 film (Fig. 11(f)). In PTB7-Th:DFBzE-RC2, the (100) peak from DFBzE- RC2 and PTB7-Th appeared at $q_z$=0.419 Å$^{-1}$ ($d$= 14.981 Å) and π-π interaction peak was observed at $q_z$=1.730 Å$^{-1}$ ($d$=3.631 Å). Additionally, peaks observed at $q_z$=1.300 Å$^{-1}$ ($d$=4.833 Å) and $q_y$=1.724 Å$^{-1}$ ($d$=3.644 Å) can be assigned to the crystal packing of DFBzE-RC2 molecules. Therefore, PTB7-Th:DFBzE- RC2 film exhibited a moderately-mixed phase, while the electron-donor and electron-acceptor materials formed their own domains. Although the degree of phase separation in each blend film differs, the results from blend film AFM, TEM, and GIWAXS suggest that a certain amount of phase separation exists in all the blend films.

### 2.4. Carrier Mobility

The hole and electron mobilities ($\mu_h$ and $\mu_e$) of the PTB7-Th:NFA blend films were calculated using the space charge-limited current (SCLC) model. Current density-voltage curves of hole-only and electron-only devices are shown in Fig. 13(a) and Fig. 13(b), and the obtained carrier mobilities are summarized in Table 5. Among the four kinds of devices, PTB7-Th: DFBzO-RC2 device showed the highest $\mu_h$ and $\mu_e$ of $3.19\times10^{-4}$ cm$^2$ V$^{-1}$ s$^{-1}$ and $7.11\times10^{-5}$ cm$^2$ V$^{-1}$ s$^{-1}$, respectively. The high carrier mobilities observed in PTB7-Th:DFBzO-RC2 device suggests that branch- like aggregates observed in the TEM data of PTB7-Th: DFBzO-RC2 blend film (Fig. 9(c)) may have acted as a good pathway for charge carrier transport. However, the rough morphology and too big phase separation of PTB7-Th:DFBzO-RC2 film was detrimental to device

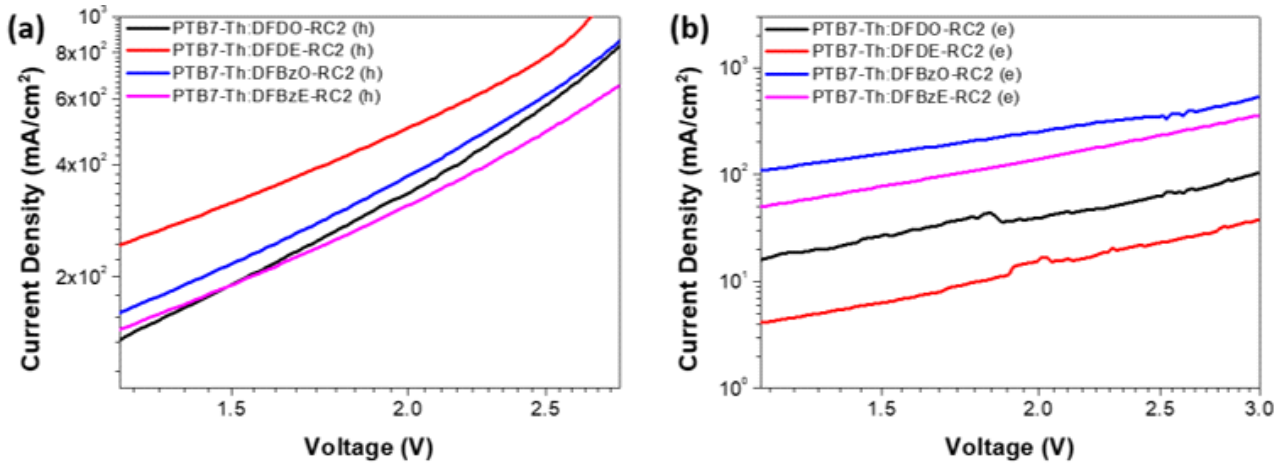


**Fig. 13.** Space charge-limited current density-voltage curves of (a) hole (h)-only devices and (b) electron (e)-only devices of PTB7-Th:DFDO-RC2, PTB7-Th:DFDE-RC2, PTB7-Th:DFBzO-RC2, and PTB7-Th:DFBzE-RC2 blends.

**Table 5.** Summary of hole and electron mobilities of PTB7-Th:DFDO-RC2, PTB7-Th:DFDE-RC2, PTB7-Th: DFBzO-RC2, and PTB7-Th:DFBzE-RC2 blend films

| Photoactive layer | $\mu_h$ ($cm^2$ $V^{-1}$ $s^{-1}$) | $\mu_e$ ($cm^2$ $V^{-1}$ $s^{-1}$) | $\mu_h/\mu_e$ ratio |
|---|---|---|---|
| PTB7-Th:DFDO-RC2 | $6.20(\pm1.78)\times10^{-4}$ | $1.84(\pm0.35)\times10^{-5}$ | 33.55 |
| PTB7-Th:DFDE-RC2 | $5.34(\pm0.60)\times10^{-4}$ | $4.98(\pm1.55)\times10^{-6}$ | 107.19 |
| PTB7-Th:DFBzO-RC2 | $3.19(\pm0.52)\times10^{-4}$ | $7.11(\pm0.61)\times10^{-5}$ | 4.49 |
| PTB7-Th:DFBzE-RC2 | $7.19(\pm1.53)\times10^{-5}$ | $4.43(\pm0.53)\times10^{-5}$ | 1.62 |

performance. Comparing the PTB7-Th: DFDO-RC2 device ($\mu_h$=6.20×$10^{-4}$ $cm^2$ $V^{-1}$ $s^{-1}$ and $\mu_e$= 1.84×$10^{-5}$ $cm^2$ $V^{-1}$ $s^{-1}$) with the PTB7-Th:DFDE-RC2 device ($\mu_h$= 5.34×$10^{-4}$ $cm^2$ $V^{-1}$ $s^{-1}$ and $\mu_e$=4.98× $10^{-6}$ $cm^2$ $V^{-1}$ $s^{-1}$), both $\mu_h$ and $\mu_e$ were higher in the PTB7-Th: DFDO-RC2 device, but a higher PCE was observed in PTB7-Th:DFDE-RC2 device. This is because the PTB7-Th: DFDE-RC2 device has better surface morphology and a larger HOMO-HOMO energy offset between PTB7-Th and DFDE-RC2, affecting photovoltaic performance more significantly. The PTB7 -Th:DFBzE-RC2 device ($\mu_h$=7.19×$10^{-5}$ $cm^2$ $V^{-1}$ $s^{-1}$ and $\mu_e$=4.43×$10^{-5}$ $cm^2$ $V^{-1}$ $s^{-1}$), which showed the highest PCE, revealed the most balanced hole-electron mobility ratio ($\mu_h/\mu_e$) of near 1. Balanced carrier transport improves charge collection at each electrode with reduced bimolecular recombination.

## 3. CONCLUSION

In conclusion, we have designed and synthesized four new small electron-acceptor molecules DFDO-RC2, DFDE-RC2, DFBzO-RC2, and DFBzE-RC2. DFBzO-RC2 and DFBzE-RC2 exhibited down-shifted HOMO levels compared to DFDO-RC2 and DFDE-RC2, which led to greater HOMO-HOMO energy offsets with PTB7-Th and thus induced more efficient exciton separation at the interface. Moreover, the DFBz series molecules showed higher extinction coefficients in the visible region than the DFD molecules, contributing to the $J_{sc}$ increase. Compared to the relatively more well-mixed phase observed in the DFD series blend films, the DFBz series blend films demonstrated a higher degree of phase separation with increased crystallinity in the blend films. PTB7-Th:DFBz-RC2 blend film revealed the most optimal morphology among the four PTB7-Th:NFA blend films. Therefore, with a simple change to DFBz in the core structure, the PTB7-Th:DFBzE-RC2 device exhibited a significant increase in PCE (4.85%), with a high $V_{oc}$ of 1.07 eV and a very low $E_{loss}$ of 0.51 eV, while the DFD series devices obtained low power conversion efficiencies (1.30%). Overall, this work demonstrates how the simple change of backbone structure influences the molecular energy level, molecular crystallinity, and morphology. Also, it shows how alkyl chain type affects the molecular interaction in the molecular-only and PTB7-Th:NFA blend films. These understandings provide insights into developing future high-performance non-fullerene acceptor molecules and improving OPV performance.

## ABBREVIATIONS

BHJ: Bulk heterojunction

$PC_{61}BM$: Phenyl-$C_{61}$-butyric acid methyl ester
$PC_{71}BM$: Phenyl-$C_{71}$-butyric acid methyl ester
NFAs: Non-fullerene acceptors
OPV: Organic photovoltaic
PCEs: Power conversion efficiency
$V_{oc}$: Open circuit voltage
IR: Near-infrared
$J_{sc}$: Short circuit current
D: Electron-donor
A: Electron-acceptor
HOMO: Highest occupied molecular orbital
LUMO: Lowest unoccupied molecular orbital
F: Difluorobenzodiathiazole
RC2: 3-Ethylrhodanine
O: Octyl
E: 2-Ethylhexyl
FBz: Difluorobenzene
MALDI-TOF-MS: Matrix-assisted laser desorption ionization mass spectrometer
DFT: Density functional theory
$E_g^{DFT}$: Bandgaps obtained from DFT
CV: Cyclic voltammetry
$E_g^{EC}$: Bandgaps obtained from CV
UV: Ultraviolet
RT: Room temperature
$E_g^{opt}$: Optical bandgaps
DSC: Differential scanning calorimetry
$T_m$: Melting temperature
$T_c$: Crystallization temperature
$L_c$: Coherence length
GIWAXS: Grazing-incidence x-ray scattering
EQE: External quantum efficiency
$E_{loss}$: Energy loss
FF: Fill factor
TEM: Transmission electron microscopy
AFM: Atomic force microscopy
RMS: Root mean square
$\mu_h$: Hole mobility
$\mu_e$: Electron mobility
SCLC: Space charge-limited current

## SUPPLEMENTARY INFORMATIOM

NMR spectra, MALDI data, Cyclic voltammogram of PTB7-Th, GIWAXS line-cut profiles, UV-vis absorption spectra of blend films and pristine PTB7-Th film. The online version contains supplementary material available at https://doi.org/10.56767/jfpe.2023.2.1.119

## ACKNOWLEDGEMENTS

This work was supported by the National Research Foundation (NRF-2021M3D1A2049323 and 2023R1A2C3006550) of the Ministry of Science and ICT.

**Author Contributions**

KKM, KBS were involved in experiments, analysis, and discussion. KKM, KBS drafted the manuscript. All authors read and approved the final manuscript.

**Funding**

This work was supported by the National Research Foundation (NRF-2021M3D1A2049323, 2023R1A2C3006550) of the Ministry of Science and ICT.

**Declarations of Competing Interests**

The authors declare that they have no competing interests.

## REFERENCES

[1] Ma, W.; Tumbleston, J. R.; Wang, M.; Gann, E.; Huang, F.; Ade, H. Domain Purity, Miscibility, and Molecular Orientation at Donor/Acceptor Interfaces in High Performance Organic Solar Cells: Paths to Further Improvement. Adv. Energy Mater. 2013, 3, 864-872.

[2] Jamieson, F. C.; Domingo, E. B.; McCarthy-Ward, T.; Heeney, M.; Stingelin, N.; Durrant, J. R. Fullerene Crystallisation as a Key Driver of Charge Separation in Polymer/Fullerene Bulk Heterojunction Solar Cells. Chem. Sci. 2012, 3, 485-492.

[3] Ballantyne, A. M.; Ferenczi, T. A. M.; Campoy-Quiles, M.; Clarke, T. M.; Maurano, A.; Wong, K. H. et al. Understanding the Influence of Morphology on Poly(3-Hexylselenothiophene):PCBM Solar Cells. Macromolecules. 2010, 43 (3), 1169-1174.

[4] van Duren, J. K. J.; Yang, X.; Loos, J.; Bulle-Lieuwma, C. W. T.; Sieval, A. B.; Hummelen, J. C. et al. Relating the Morphology of Poly(p-Phenylene vinylene)/Methanofullerene Blends to Solar- Cell Performance. Adv. Funct. Mater. 2004, 14 (5), 425-434.

[5] Lin, Y.; Wang, J.; Zhang, Z. G.; Bai, H.; Li, Y.; Zhu, D. et al. An Electron Acceptor Challenging Fullerenes for Efficient Polymer Solar Cells. Adv. Mater. 2015, 27 (7), 1170-1174.

[6] Yuan, J.; Zhang, Y.; Zhou, L.; Zhang, G.; Yip, H.; Lau, T. et al. Single-Junction Organic Solar Cell with over 15% Efficiency Using Fused-Ring Acceptor with Electron-Deficient Core. Joule. 2019, 3 (4), 1140-1151.

[7] Li, C.; Zhou, J.; Song, J.; Xu, J.; Zhang, H.; Zhang, X. et al. Non-Fullerene Acceptors with Branched Side Chains and Improved Molecular Packing to Exceed 18% Efficiency in Organic Solar Cells. Nat. Energy. 2021, 6, 605-613.

[8] Lee, Y.; Raju, T. B.; Yeom, H.; Gopikrishna, P.; Kim, K.; Cho, H. W. et al. Alkyl Chain Engineering of Low Bandgap Non-Fullerene Acceptors for High-Performance Organic Solar Cells: Branched vs. Linear Alkyl Side Chains. Polymers. 2022, 14 (18), 3812.

[9] Liu, Q.; Jiang, Y.; Jin, K.; Qin, J.; Xu, J.; Li, W. et al. 18% Efficiency Organic Solar Cells. Sci. Bull. 2020, 65 (4), 272-275.

[10] Qi, F.; Jiang, K.; Lin, F.; Wu, Z.; Zhang, H.; Gao, W. et al. Over 17% Efficiency Binary Organic Solar Cells with Photoresponses Reaching 1000 nm Enabled by Selenophene-Fused Nonfullerene Acceptors. ACS Energy Lett. 2021, 6 (1), 9-15.

[11] Zhu, C.; Yuan, J.; Cai, F.; Meng, L.; Zhang, H.; Chen, H. et al. Tuning the Electron-Deficient Core of a Non-Fullerene Acceptor to Achieve over 17% Efficiency in a Single-Junction Organic Solar Cell. Energy Environ. Sci. 2020, 13 (8), 2459-2466.

[12] Cui, Y.; Yao, H.; Zhang, J.; Xian, K.; Zhang, T.; Hong, L. et al. Single-Junction Organic Photovoltaic Cells with Approaching 18% Efficiency. Adv. Mater. 2020, 32 (19), 1908205.

[13] Yang, D.; Wang, Y.; Sano, T.; Gao, F.; Sasabe, H.; Kido, J. A Minimal Non-Radiative Recombination Loss for Efficient Non-Fullerene All-Small-Molecule Organic Solar Cells with a Low

Energy Loss of 0.54 eV and High Open-Circuit Voltage of 1.15 V. J. Mater. Chem. A 2018, 6 (28), 13918-13924.

[14] Tang, A.; Xiao, B.; Chen, F.; Zhang, J.; Wei, Z.; Zhou, E. The Introduction of Fluorine and Sulfur Atoms into Benzotriazole-Based p-Type Polymers to Match with a Benzotriazole-Containing n-Type Small Molecule: “The Same-Acceptor-Strategy” to Realize High Open-Circuit Voltage. Adv. Energy Mater. 2018, 8 (25), 1801582.

[15] An, N.; Cai, Y.; Wu, H.; Tang, A.; Zhang, K.; Hao, X. et al. Solution-Processed Organic Solar Cells with High Open-Circuit Voltage of 1.3 V and Low Non-Radiative Voltage Loss of 0.16 V. Adv. Mater. 2020, 32 (39), 2002122.

[16] Luo, Z.; Ma, R.; Liu, T.; Yu, J.; Xiao, Y.; Sun, R. et al. Fine-Tuning Energy Levels via Asymmetric End Groups Enables Polymer Solar Cells with Efficiencies over 17%. Joule 2020, 4 (6), 1236-1247.

[17] Raju, T. B.; Cho, H. W.; Gopikrishna, P.; Lee, Y.; Kim, J. Y.; Kim, B. Positional Effect of the 2-Ethylhexyl Carboxylate Side Chain on the Thiophene π-Bridge of Nonfullerene Acceptors for Efficient Organic Solar Cells. ACS Appl. Energy Mater. 2021, 4 (10), 11675-11683.

[18] Yun, J. H.; Park, S.; Heo, J. H.; Lee, H. S.; Yoon, S.; Kang, J. et al. Enhancement of Charge Transport Properties of Small Molecule Semiconductors by Controlling Fluorine Substitution and Effects on Photovoltaic Properties of Organic Solar Cells and Perovskite Solar Cells. Chem. Sci. 2016, 7 (11), 6649-6661.

[19] Zhang, H.; Yao, H.; Hou, J.; Zhu, J.; Zhang, J.; Li, W. et al. Over 14% Efficiency in Organic Solar Cells Enabled by Chlorinated Nonfullerene Small-Molecule Acceptors. Adv. Mater. 2018, 30 (28), 1800613.

[20] Chen, S.; Feng, L.; Jia, T.; Jing, J.; Hu, Z.; Zhang, K. et al. High-Performance Polymer Solar Cells with Efficiency over 18% Enabled by Asymmetric Side Chain Engineering of Non-Fullerene Acceptors. Sci. China Chem. 2021, 64, 1192-1199.

[21] Holliday, S.; Ashraf, R. S.; Wadsworth, A.; Baran, D.; Yousaf, S. A.; Nielsen, C. B. et al. High-Efficiency and Air-Stable P3HT-Based Polymer Solar Cells with a New Non-Fullerene Acceptor. Nat. Commun. 2016, 7, 11585.

[22] Baran, D.; Ashraf, R. S.; Hanifi, D. A.; Abdelsamie, M. Gasparini, N.; Rohr, J. A. et al. Reducing the Efficiency-Stability-Cost Gap of Organic Photovoltaics with Highly Efficient and Stable Small Molecule Acceptor Ternary Solar Cells. Nat. Mater. 2017, 16, 363-369.

[23] Du, X.; Heumueller, T.; Gruber, W.; Classen, A.; Unruh, T.; Li, N. et al. Efficient Polymer Solar Cells Based on Non-Fullerene Acceptors with Potential Device Lifetime Approaching 10 Years. Joule 2019, 3 (1), 215-226.

[24] Cha, H.; Wu, J.; Wadsworth, A.; Nagitta, J.; Limbu, S.; Pont, S. et al. An Efficient, "Burn in" Free Organic Solar Cell Employing a Nonfullerene Electron Acceptor. Adv. Mater. 2017, 29 (33), 1701156.

[25] Gopikrishna, P.; Choi, H.; Kim, D. H.; Hwang, J. H.; Lee, Y.; Jung, H. et al. Impact of Symmetry-Breaking of Non-Fullerene Acceptors for Effi-

cient and Stable Organic Solar Cells. Chem. Sci. 2021, 12 (42), 14083-14097.

[26] Zhao, W.; Li, S.; Yao, H.; Zhang, S.; Zhang, Y.; Yang, B. et al. Molecular Optimization Enables over 13% Efficiency in Organic Solar Cells. J. Am. Chem. Soc. 2017, 139 (21), 7148-7151.

[27] Sun, J.; Ma, X.; Zhang, Z.; Yu, J.; Zhou, J.; Yin, X. et al. Dithieno[3,2-b:2',3'-d]pyrrol Fused Nonfullerene Acceptors Enabling Over 13% Efficiency for Organic Solar Cells. Adv. Mater. 2018, 30 (16), 1707150.

[28] Fei, Z.; Eisner, F. D.; Jiao, X.; Azzouzi, M.; Rohr, J. A.; Han, Y. et al. An Alkylated Indacenodithieno[3,2-b]thiophene-Based Nonfullerene Acceptor with High Crystallinity Exhibiting Single Junction Solar Cell Efficiencies Greater than 13% with Low Voltage Losses. Adv. Mater. 2018, 30 (8), 1705209.

[29] Yang, B.; Li, J.; Wu, C.; Zhang, H.; Pan, A.; Chen, J. Non-Fullerene Acceptors for Large-Open-Circuit-Voltage and High-Efficiency Organic Solar Cells. Mater. Today Nano 2018, 1, 47-59.

[30] Zhang, M.; Guo, X.; Zhang, S.; Hou, J. Synergistic Effect of Fluorination on Molecular Energy Level Modulation in Highly Efficient Photovoltaic Polymers. Adv. Mater. 2014, 26 (7), 1118-1123.

[31] Kawashima, K.; Fukuhara, T.; Suda, Y.; Suzuki, Y.; Koganezawa, T.; Yoshida, H. et al. Implication of Fluorine Atom on Electronic Properties, Ordering Structures, and Photovoltaic Performance in Naphthobisthiadiazole-Based Semiconducting Polymers. J. Am. Chem. Soc. 2016, 138 (32), 10265-10275.

[32] Reichenbacher, K.; Suss, H. I.; Hulliger, J. Fluorine in Crystal Engineering- "The Little Atom that Could". Chem. Soc. Rev. 2005, 34 (1), 22-30.

[33] Bronstein, H.; Frost, J. M.; Hadipour, A.; Kim, Y.; Nielsen, C. B.; Ashraf, R. S. et al. Effect of Fluorination on the Properties of a Donor-Acceptor Copolymer for Use in Photovoltaic Cells and Transistors. Chem. Mater. 2013, 25 (3), 277-285.

[34] Ock, J.; Kim, D.; Kim, H.; Jung, H.; Son, H. J.; Ko, M. J. et al. Balancing Intermolecular Interactions by Variation of Pendent Alkyl Chains for High Performance Organic Photovoltaics. Dyes Pigm. 2017, 137, 445-455.

[35] Nguyen, T. L.; Choi, H.; Ko, S. J.; Uddin, M. A.; Walker, B.; Yum, S. et al. Semi-Crystalline Photovoltaic Polymers with Efficiency Exceeding 9% in a ∼300 nm Thick Conventional Single-Cell Device. Energy Environ. Sci. 2014, 7 (9), 3040-3051.

[36] Zheng, Z.; Awartani, O. M.; Gautam, B.; Liu, D.; Qin, Y.; Li, W. et al. Efficient Charge Transfer and Fine-Tuned Energy Level Alignment in a THF-Processed Fullerene-Free Organic Solar Cell with 11.3% Efficiency. Adv. Mater. 2017, 29 (5), 1604241.

[37] Holliday, S.; Ashraf, R. S.; Nielsen, C. B.; Kirkus, M.; Rohr, J. A.; Tan, C. H. et al. A Rhodanine Flanked Nonfullerene Acceptor for Solution-Processed Organic Photovoltaics. J. Am. Chem. Soc. 2015, 137 (2), 898-904.

[38] Más-Montoya, M.; Janssen, R. A. The Effect of H-and J-Aggregation on the Photophysical and Photovoltaic Properties of Small Thiophene-

Pyridine-DPP Molecules for Bulk-Heterojunction Solar Cells. Adv. Funct. Mater. 2017, 27 (16), 1605779.

[39] Lee, D. C.; Jeong, Y.; Brownell, L. V.; Velasco, J. E.; Robins, K. A.; Lee, Y. Theory Guided Systematic Molecular Design of Benzothiadiazole-Phenazine Based Self-Assembling Electron-Acceptors. RSC Adv. 2017, 7 (39), 24105-24112.

[40] Jung, M.; Yoon, Y.; Park, J. H.; Cha, W.; Kim, A.; Kang, J. et al. Nanoscopic Management of Molecular Packing and Orientation of Small Molecules by a Combination of Linear and Branched Alkyl Side Chains. ACS Nano 2014, 8 (6), 5988-6003.

[41] Nayak, P. K.; Cahen, D. Updated Assessment of Possibilities and Limits for Solar Cells. Adv. Mater. 2014, 26 (10), 1622-1628.

[42] Yao, J.; Kirchartz, T.; Vezie, M. S.; Faist, M. A.; Gong, W.; He, Z. et al. Quantifying Losses in Open-Circuit Voltage in Solution-Processable Solar Cells. Phys. Rev. Applied 2015, 4, 014020.

[43] Zhang, H.; Li, S.; Xu, B.; Yao, H.; Yang, B.; Hou, J. Fullerene-Free Polymer Solar Cell Based on a Polythiophene Derivative with an Unprecedented Energy Loss of Less than 0.5 eV. J. Mater. Chem. A 2016, 4 (46), 18043-18049.

[44] An, Q.; Gao, W.; Zhang, F.; Wang, J.; Zhang, M.; Wu, K. et al. Energy Level Modulation of Non-Fullerene Acceptors Enables Efficient Organic Solar Cells with Small Energy Loss. J. Mater. Chem. A 2018, 6 (6), 2468-2475.

[45] Ye, P.; Chen, Y.; Wu, J.; Wu, X.; Yu, S.; Xing, W. et al. Wide Bandgap Small Molecular Acceptors for Low Energy Loss Organic Solar Cells. J. Mater. Chem. C 2017, 5 (47), 12591-12596.

[46] Xiao, J.; Chen, Z.; Zhang, G.; Li, Q.; Yin, Q.; Jiang, X. et al. Efficient Device Engineering for Inverted Non-Fullerene Organic Solar Cells with Low Energy Loss. J. Mater. Chem. C 2018, 6 (16), 4457-4463.

[47] Hadmojo, W. T.; Wibowo, F. T. A.; Ryu, D. Y.; Jung, I. H.; Jang, S. Y. Fullerene-Free Organic Solar Cells with an Efficiency of 10.2% and an Energy Loss of 0.59 eV Based on a Thieno[3,4-c] Pyrrole-4,6-dione-Containing Wide Band Gap Polymer Donor. ACS Appl. Mater. Interfaces 2017, 9 (38), 32939-32945.

[48] He, B.; Yang, B.; Kolaczkowski, M. A.; Anderson, C. A.; Klivansky, L. M.; Chen, T. L. et al. Molecular Engineering for Large Open-Circuit Voltage and Low Energy Loss in Around 10% Non-fullerene Organic Photovoltaics. ACS Energy Lett. 2018, 3 (4), 1028-1035.

[49] Yang, J.; Chen, F.; Hu, J.; Geng, Y.; Zeng, Q.; Tang, A. et al. Planar Benzofuran Inside-Fused Perylenediimide Dimers for High VOC Fullerene-Free Organic Solar Cells. ACS Appl. Mater. Interfaces 2019, 11 (4), 4203-4210.